

A full-scale roller-rig for railway vehicles: multibody modelling and Hardware In the Loop architecture

R. Conti¹ · E. Meli¹ · A. Ridolfi¹

Received: 27 February 2015 / Accepted: 25 January 2016 / Published online: 24 February 2016
© Springer Science+Business Media Dordrecht 2016

Abstract In this paper an innovative Hardware In the Loop (HIL) architecture to test braking onboard subsystems on full-scale roller-rigs is described. The new approach allows reproducing on the roller-rig a generic wheel–rail adhesion pattern (especially degraded adhesion conditions) without sliding and, consequently, wear between the roller and wheel surfaces. The presented strategy is also adopted by the innovative full-scale roller-rig of the Railway Research and Approval Center of Firenze-Osmannoro (Italy); the new roller-rig has been built by Trenitalia S.p.A. and is owned by SIMPRO S.p.A. At this initial phase of the research activity, to effectively validate the proposed approach, a complete multibody model of the HIL system has been developed. The numerical model is based on the real characteristics of the components provided by Trenitalia and makes use of an innovative wheel–roller contact model. The results coming from the simulation model have been compared to the experimental data provided by Trenitalia and relative to on-track tests performed in Velim, Czech Republic, with a UIC-Z1 coach equipped with a fully-working WSP system. The preliminary validation performed with the HIL model highlights the good performance of the HIL strategy in reproducing on the roller-rig the complex interaction between degraded adhesion conditions and railway vehicle dynamics during the braking manoeuvre.

Keywords Full-scale roller-rig · Wheel–roller contact · Wheel–rail contact · Hardware In the Loop · Railway vehicles

✉ E. Meli
enrico.meli@unifi.it

R. Conti
roberto.conti@unifi.it

A. Ridolfi
a.ridolfi@unifi.it

¹ Department of Industrial Engineering, University of Florence, Via di S.Marta n. 3, 50139 Firenze, Italy

1 Introduction

Nowadays the longitudinal train dynamics is almost totally controlled by onboard subsystems, such as Wheel Slide Protection (WSP) braking devices. The study and the development of these systems are fundamental for the vehicle safety, especially at high speeds and under degraded adhesion conditions. On-track tests are currently quite expensive in terms of infrastructure and vehicle management. Consequently, to reduce these costs, full-scale roller-rigs are traditionally employed to investigate the performances of braking subsystems [1–5]. However, in the presence of degraded adhesion, the use of roller-rigs is still limited to few applications (see, for example, full-scale roller-rigs for the study of the wear [6], HIL systems for WSP tests [7] and full-scale roller-rigs for locomotive tests [7, 8]) because the high slidings between rollers and wheelsets produce wear of the rolling surfaces. This circumstance is very dangerous and not acceptable: the flange wear can lead to the vehicle derailment while the tread wear can produce hunting instability of the vehicle. Furthermore, the wheel flats may generate unsafe vibrations of the vehicle on the roller-rig. Finally, the wear of the rolling surfaces deeply affects the maintenance costs: the rollers have to be frequently turned or substituted.

On the other hand, few applications making use of scaled roller-rigs can be found in the literature. In this regard, interesting HIL systems to study railway traction and braking onboard subsystems have been developed during the last years by the Polytechnic of Turin and Central Queensland University [9–12].

In this work an innovative Hardware In the Loop (HIL) architecture to test braking onboard subsystems on full-scale roller-rigs is presented by the authors. The new strategy allows reproducing on the roller-rig a generic wheel–rail adhesion pattern and, in particular, degraded adhesion conditions (characterised by adhesion coefficient values equal or less than 0.10). More in detail, the new control architecture performs a simulation of mechanical impedance: the roller motors are controlled to recreate, on the wheelsets, the same angular velocities, applied torques and tangential efforts calculated by the model of a reference virtual railway vehicle moving on the real track under degraded adhesion conditions. The new architecture allows the achievement of this goal by only controlling the roller motors and without having sliding between wheelsets and rollers (and consequently without wear of the contact surfaces). In fact, since the real adhesion coefficient between the rollers and wheelsets surfaces is far higher than the simulated one (greater than 0.40), negligible sliding occurs and almost pure rolling conditions are always present between them.

At this initial phase of the research activity, the described strategy has been completely simulated in the Matlab-Simulink environment [13] through an accurate multibody model of the whole HIL architecture. The system model comprises an innovative contact model to describe the wheel–roller interaction and is developed according to the real characteristics provided by Trenitalia. The proposed approach has been preliminarily validated through a comparison with the experimental data provided by Trenitalia and relative to on-track tests performed on a straight railway track (in Velim, Czech Republic) with a UIC-Z1 coach equipped with a fully-working WSP system [14–16]. This initial validation carried out through the HIL model highlights the good performance of the HIL strategy in reproducing on the roller-rig the complex interaction between degraded adhesion conditions and railway vehicle dynamics during the braking manoeuvre.

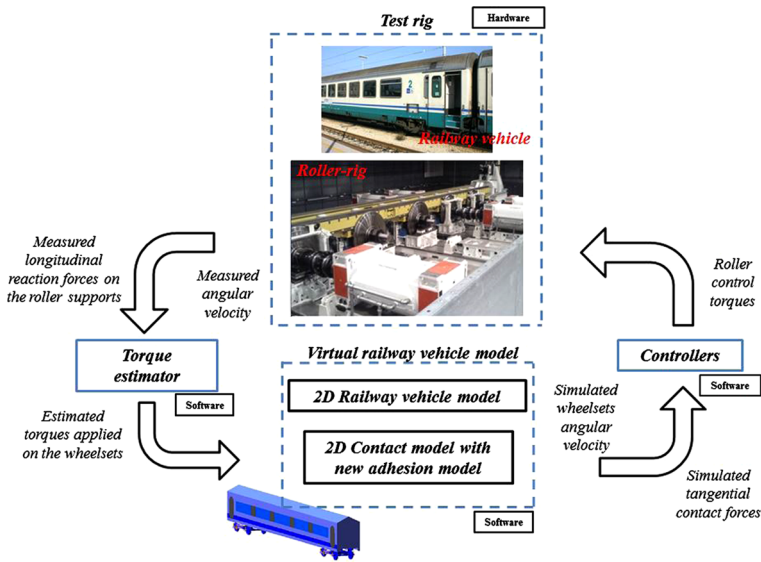


Fig. 1 General architecture of the HIL system

2 General architecture of the HIL system

In this section the architecture of the Firenze-Osmannoro HIL system is briefly described. Figure 1 schematically shows the main parts of the architecture (both for the hardware and the software components). The models used to simulate all these parts will be better explained in Sect. 3.

The architecture comprises four main elements:

1. The *test-rig (hardware)* composed of two main parts: the UIC-Z1 railway vehicle (equipped with the WSP system) [14, 15] and the Firenze-Osmannoro roller-rig (with the innovative actuation system developed in collaboration with SICME and based on IPM synchronous motor with high performance) [17, 18]. The inputs of the test-rig are the roller control torques while the outputs are the longitudinal reaction forces measured on the roller supports and the measured angular velocities of the rollers;
2. The *virtual railway vehicle model (software)* representing the model used to simulate the vehicle behaviour on the rails under different adhesion conditions and designed for a real-time implementation. This 2D multibody model simulates the longitudinal dynamics of the vehicle while an innovative 2D adhesion model [19] permits an accurate reproduction of the real behaviour of the adhesion coefficient during braking phases under degraded adhesion conditions. The inputs are the estimated torques on the wheelsets and the outputs are the simulated wheelset angular velocities and the tangential contact forces on the wheelsets;
3. The *controllers (software)* reproduce on the roller-rig the same dynamical behaviour of the virtual train model (through the roller control torques) in terms of wheelset angular velocities, applied torques and, consequently, tangential forces. Due to the HIL system nonlinearities, a sliding mode approach has been adopted for the controllers [20, 21];
4. The *torque estimators (software)* – the data measured by the sensors installed on the roller-rig are only the roller angular velocities and the longitudinal reaction forces on the roller supports. No sensors will be placed on the vehicle to speed up the set up process. Starting from these quantities, this block estimates the torques applied on the wheelsets.

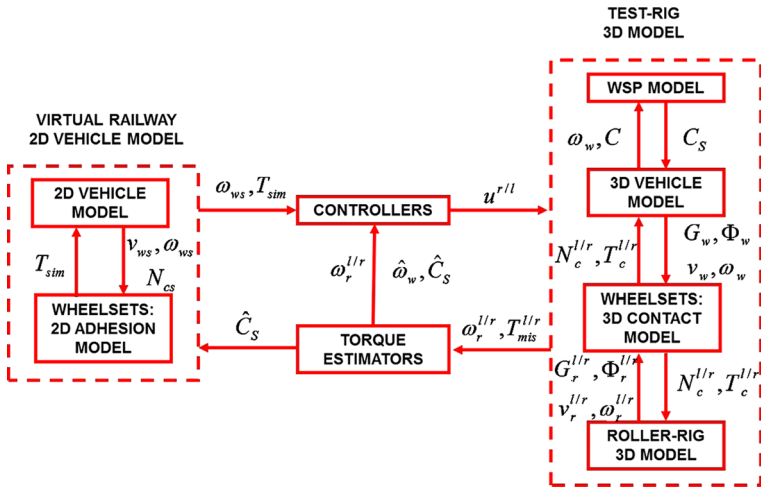


Fig. 2 Interactions among the models of the various HIL architecture components

Fig. 3 The UIC-Z1 wagon



3 Modelling of the Firenze-Osmannoro HIL system

In this section the models of the HIL system presented in the previous section (both hardware and software parts) and of all the components of the HIL architecture will be explained in detail. The flow of the data among the model parts is shown in Fig. 2.

3.1 The test-rig model

The inputs of the whole test-rig model are the 8 roller control torques u^l, u^r (left and right) evaluated by the controllers to reproduce on the test-rig the same dynamical behaviour of the virtual railway model. The outputs are the 8 roller angular velocities ω_r^l, ω_r^r and the longitudinal reaction forces T_{mis}^l, T_{mis}^r measured on the roller supports. The test-rig model is composed of four parts (Fig. 2):

3.1.1 The vehicle model

The considered railway vehicle is the UIC-Z1 wagon (illustrated in Figs. 3 and 4); its geometrical and physical characteristics are provided by Trenitalia S.p.A. [14].

Fig. 4 Multibody vehicle model

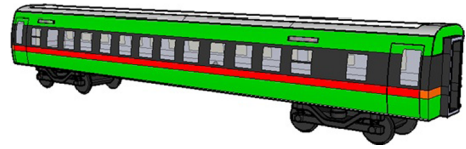


Fig. 5 Primary and secondary suspensions

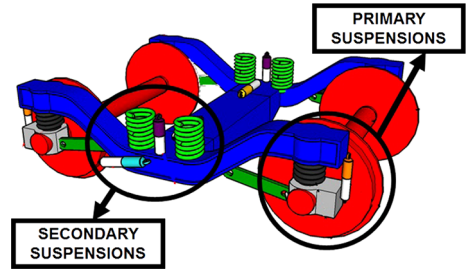


Table 1 Main characteristics of the railway vehicle

Parameter	Units	Value
Total mass	[kg]	≈43000
Wheel arrangement	–	2–2
Bogie wheelbase	[m]	2.56
Bogie distance	[m]	19
Wheel diameter	[m]	0.89
Primary suspensions frequency	[Hz]	≈4.5
Secondary suspensions frequency	[Hz]	≈0.8

Table 2 Inertial properties of the rigid bodies

Body	Mass [kg]	I_{xx} [kg m ²]	I_{yy} [kg m ²]	I_{zz} [kg m ²]
Carbody	≈29000	76400	1494400	1467160
Bogie	≈3000	2400	1900	4000
Wheelset	≈1300	800	160	800
Axlebox	≈200	3	12	12

The wagon is composed of one carbody, two bogie frames, eight axleboxes and four wheelsets. The primary suspension, including springs, dampers and axlebox bushings, connects the bogie frame to the four axleboxes while the secondary suspension, including springs, dampers, lateral bump-stops, anti-roll bar and traction rod, connects the carbody to the bogie frames (see Fig. 5). In Table 1, the main properties of the railway vehicle are given. The multibody vehicle model takes into account all the degrees of freedom (DOFs) of the system bodies (one carbody, two bogie frames, eight axleboxes, and four wheelsets). Considering the kinematic constraints that link the axleboxes and the wheelsets (cylindrical 1DOF joints) and without including the wheel–rail contacts, the whole system has 50 DOFs. The main inertial properties of the bodies are summarised in Table 2 [14].

Both the primary suspension (springs, dampers and axlebox bushings) and the secondary suspension (springs, dampers, lateral bump-stops, anti-roll bar and traction rod) have been modelled through 3D visco-elastic force elements able to describe all the main nonlinearities

Table 3 Main linear elastic characteristics of the two stage suspensions

Element	Transl. Stiff. x [N/m]	Transl. Stiff. y [N/m]	Transl. Stiff. z [N/m]	Rotat. Stiff. x [N m/rad]	Rotat. Stiff. y [N m/rad]	Rotat. Stiff. z [N m/rad]
Springs of the primary suspension	844000	844000	790000	10700	10700	0
Springs of the secondary suspension	124000	124000	340000	0	0	0
Axlebox bushing	$4 \cdot 10^7$	$6.5 \cdot 10^6$	$4 \cdot 10^7$	45000	9700	45000
Anti-roll bar	0	0	0	$2.5 \cdot 10^6$	0	0

of the system (see Fig. 5). In Table 3, the characteristics of the main linear elastic force elements of both the suspension stages are reported [14]. The nonlinear elastic force elements have been modelled through nonlinear functions that correlate the displacements and the relative velocities of the force elements connection points to the elastic and damping forces exchanged by the bodies. The inputs of the model are the 4 wheelset torques C_s modulated by the on board WSP and the contact forces calculated by the contact model, while the outputs are the kinematic wheelset variables transmitted to the contact model, the 4 original torques C (without the on board WSP modulation) and the 4 wheelset angular velocities ω_w . These last two outputs are not accessible by the HIL system.

3.1.2 The Wheel Slide Protection system model

The WSP device installed on the UIC-Z1 coach [15, 22] allows the control of the torques applied to the wheelsets, to prevent macro-sliding during the braking phase. In Fig. 6, the logical scheme and an image of the WSP device are shown. The inputs are the braking torques C and the wheelset velocities ω_w , while the outputs are the modulated braking torques C_s . The WSP system working principle can be divided into three different tasks: the evaluation of the reference vehicle velocity V_{ref} and acceleration a_{ref} based on the wheelset angular velocities ω_w and accelerations $\dot{\omega}_w$; the computation of the logical sliding state $state_{\text{WSP}}$ (equal to 1 if sliding occurs and 0 otherwise) and the consequent torque modulation, through a speed and an accelerometric criterion and by means of a suitable logical table [22]; the periodic braking release to bring back the perceived adhesion coefficient to the original value (often used when degraded adhesion conditions are very persistent and the WSP logic tends to drift).

3.1.3 The roller-rig model

The 3D multibody model of the roller-rig (see Fig. 7 and Table 4) consists of 8 independent rollers with a particular roller profile able to exactly reproduce the UIC60 rail pattern with different laying angles α_p [17]. The railway vehicle is axially constrained on the rollers using two axial links (front and rear) modelled by means of 3D force elements with linear stiffness and damping. The inputs of the test-rig model are the 8 torques u^l, u^r evaluated by the controllers and the contact forces calculated by the contact model; the outputs are the roller angular velocities ω_r^l, ω_r^r , the longitudinal reaction forces $T_{\text{mis}}^l, T_{\text{mis}}^r$ measured on the roller supports and the kinematic wheelset variables transmitted to the contact model. The roller-rig actuation system consists of 8 synchronous motors, especially designed and developed in cooperation with SICME [18] for this kind of application. The HIL architecture includes a direct-drive connection between the roller and the electrical machine. The

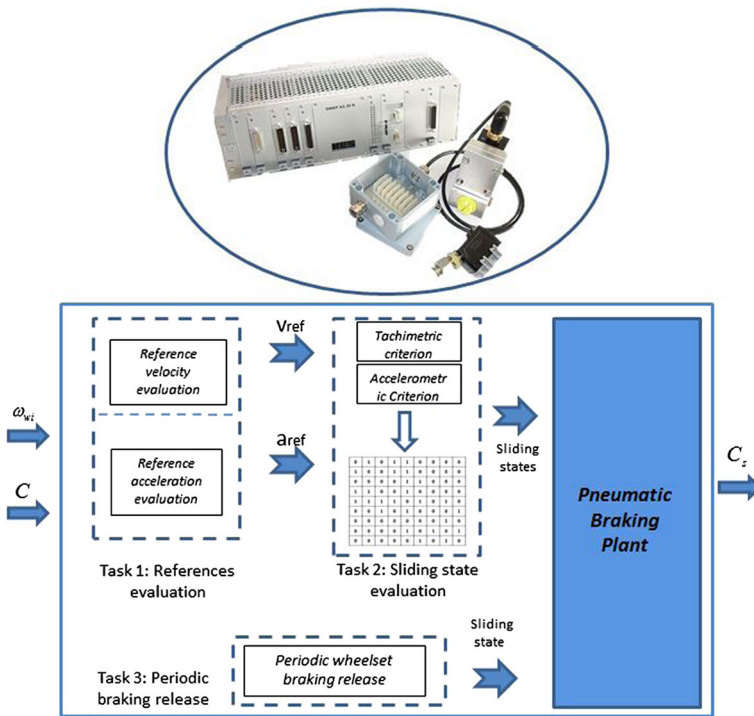
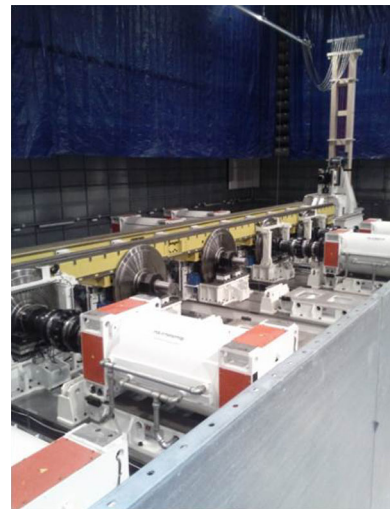


Fig. 6 WSP device and its logical scheme

Fig. 7 The right side of roller-rig system with the synchronous motors and the rollers placed in the semi-anechoic room of the Research and Approval Center of Firenze-Osmannoro



synchronous motors have high efficiency associated with high torque density and flux weakening capability. Furthermore, to reach the dynamical and robustness performances required by the railway full-scale roller-rig, the motors are designed with a multilayer-rotor characterised by a high saliency ratio ξ and Interior Permanent Magnets (IPM). The IPM motors

Table 4 Main characteristics of the roller-rig system and of the wheelsets

Parameter	Units	Value
Roller radius r_r	m	0.725
Roller mass m_r	kg	2980
Roller inertia J_r	kg m ²	705
Wheelset radius r_w	m	0.445
Wheelset mass m_w	kg	1300
Wheelset inertia J_w	kg m ²	160

are controlled in real-time through vector control techniques; more particularly, the vector control is a torque-controlled drive system in which the controller follows a desired torque [18, 23–26]. The main sensors installed on the roller-rig are the absolute encoders and the 3-axial load cells on the roller supports. These sensors are employed both in the torque estimators and in the controllers and measure, respectively, the roller angular velocities ω_r^l , ω_r^r and the longitudinal reaction forces T_{mis}^l , T_{mis}^r on the roller supports.

3.1.4 The wheel–roller contact model

The 3D contact model evaluates the contact forces $\mathbf{N}_c^{l/r}$, $\mathbf{T}_c^{l/r}$ for all the 8 wheel–roller pairs starting from the kinematic variables of the wheelsets and of the rollers: their positions \mathbf{G}_w , $\mathbf{G}_r^{l/r}$, orientations ϕ_w , $\phi_r^{l/r}$, velocities \mathbf{v}_w , $\mathbf{v}_r^{l/r}$ and angular velocities ω_w , $\omega_r^{l/r}$. The wheel–roller contact model is an improvement of previous models developed for the wheel–rail pair and detailed in [27–29]. The contact model can be logically divided into two parts: the contact point detection between two revolute surfaces and the calculation of the normal and tangential contact forces.

There are different strategies in the literature [30, 31] to find the contact points. The one adopted in the roller-rig simulator is based on semi-analytical procedures and satisfies the following requirements:

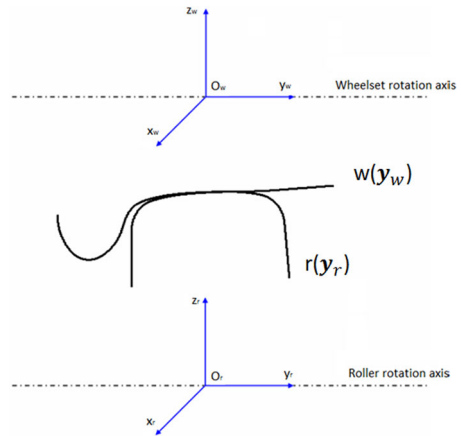
- The contact detection algorithm between revolute surfaces is fully 3D and does not introduce simplifying assumptions on the problem geometry and kinematics;
- Generic wheel–roller profiles;
- Accurate management of the multiple contact points without limits on the point number;
- High computational efficiency needed for the online implementation within multibody models.

The research of the contact points is based on the consideration that the contact points between the wheel surface and the roller surface are located where the distance between the two surfaces assumes a stationary point. The following conditions allow finding these points:

1. *Parallelism Condition* between the normal unitary vector to the roller surface and the normal unitary vector to the wheel surface;
2. *Parallelism Condition* between the normal unitary vector to the roller surface and the vector representing the distance \mathbf{d}^r between the generic point of the wheel and the rail surfaces.

Going through the details of the procedure, a fixed reference system $O_r x_r y_r z_r$ is defined, with its origin located on the roller rotation axis and the axis y_r parallel to the rotation axis (Fig. 8). The local reference system $O_w x_w y_w z_w$ is defined on the wheelset, with the axis y_w

Fig. 8 Fixed reference system and local reference system



coincident with the rotation axis of the wheelset. The origin O_w coincides with the common point between the nominal rolling plane and the wheelset axis.

The vector \mathbf{O}_w^r is the position of the local references system with respect to the fixed one and $[\mathbf{R}]$ is the rotation matrix that represents the relative orientations. In the local system, the axle can be described by a revolution surface. The generative function is indicated with $w(y_w)$.

In the local reference frame, the position of a generic point of the wheel surface is described by the following analytic expression:

$$\mathbf{p}_w^w(x_w, y_w) = \begin{bmatrix} x_w & y_w & -\sqrt{w(y_w)^2 - x_w^2} \end{bmatrix}^T, \tag{1}$$

while in the fixed reference system the same position is given by

$$\mathbf{p}_w^r(x_w, y_w) = \mathbf{O}_w^r + [\mathbf{R}]\mathbf{p}_w^w(x_w, y_w). \tag{2}$$

Similarly, the roller can be described by a revolution surface with respect to the fixed reference system (the generative function is indicated by $r(y_r)$, see Fig. 8). The main difference with respect to the method presented in [27–29] is obviously the geometry of the contact bodies. Since the semi-analytic methods are based on a preliminary algebraic simplification of the above introduced geometrical conditions and since the contact geometries have necessarily different mathematical representations, the method presented in [27–29] has to be properly modified. The position of a generic point of the roller surface has the following analytic expression:

$$\mathbf{p}_r^r(x_r, y_r) = \begin{bmatrix} x_r & y_r & +\sqrt{r(y_r)^2 - x_r^2} \end{bmatrix}^T. \tag{3}$$

The outgoing normal unit vector to the wheel surface in the local system is defined by $\mathbf{n}_w^w(\mathbf{p}_w^w)$ while, in the fixed reference system, it will be

$$\mathbf{n}_w^r(\mathbf{p}_w^r) = [\mathbf{R}]\mathbf{n}_w^w(\mathbf{p}_w^w). \tag{4}$$

In the fixed reference system, the outgoing normal unitary vector to the rail surface is defined as $\mathbf{n}_r^r(\mathbf{p}_r^r)$. The complete expressions of the normal unit vectors are:

$$\mathbf{n}_w^w(\mathbf{p}_w^w) = \frac{-\left(\frac{\partial \mathbf{p}_w^w}{\partial x_w} \times \frac{\partial \mathbf{p}_w^w}{\partial y_w}\right)}{\left\| \frac{\partial \mathbf{p}_w^w}{\partial x_w} \times \frac{\partial \mathbf{p}_w^w}{\partial y_w} \right\|}, \quad \mathbf{n}_r^r(\mathbf{p}_r^r) = \frac{\left(\frac{\partial \mathbf{p}_r^r}{\partial x_r} \times \frac{\partial \mathbf{p}_r^r}{\partial y_r}\right)}{\left\| \frac{\partial \mathbf{p}_r^r}{\partial x_r} \times \frac{\partial \mathbf{p}_r^r}{\partial y_r} \right\|}. \tag{5}$$

The distance vector between two generic points belonging to the wheel surface and the roller surface is defined as

$$\mathbf{d}^r(x_w, y_w, x_r, y_r) = \mathbf{p}_w^r(x_w, y_w) - \mathbf{p}_r^r(x_r, y_r); \tag{6}$$

as can be seen, the distance vector is a function of four parameters.

The *Parallelism Conditions* can be formally written as follows:

$$\mathbf{n}_r^r(\mathbf{p}_r^r) \parallel \mathbf{n}_w^r(\mathbf{p}_w^r) \rightarrow \mathbf{n}_r^r(\mathbf{p}_r^r) \times [\mathbf{R}]\mathbf{n}_w^w(\mathbf{p}_w^w) = \mathbf{0}, \tag{7}$$

$$\mathbf{n}_r^r(\mathbf{p}_r^r) \parallel \mathbf{d}^r \rightarrow \mathbf{n}_r^r(\mathbf{p}_r^r) \times [\mathbf{R}]\mathbf{d}^r = \mathbf{0}. \tag{8}$$

These conditions could be replaced by the *Orthogonality Condition* between the tangent plane to the roller surface in \mathbf{p}_r^r and $\mathbf{d}^r(x_w, y_w, x_r, y_r)$ and the *Orthogonality Condition* between the tangent plane to the wheel surface in \mathbf{p}_w^w and $\mathbf{d}^r(x_w, y_w, x_r, y_r)$. In this case, the formulation turns out to be analytically more complicated than the previous one, and therefore it has not been employed.

The conditions defined in Eqs. (7)–(8) are an algebraic system of 6 equations (of which only 4 are independent; for example, the first two components of each vectorial equation) in 4 unknowns. However, as will be shown in the following, the original 4D system can be analytically reduced to one single scalar equation $F(y_w) = 0$ (that, at this point, can be easily solved numerically) by expressing the variables x_w, x_r, y_r as a function of y_w . The reduction of the algebraic problem dimension (from 4D to 1D) represents the most innovative feature of the algorithm; the main benefits of the new approach are:

- High computational efficiency,
- Easy management of the multiple solutions, and also
- Simplified algorithm (like the grid method) can be numerically efficient if applied to the scalar problem.

The solutions of Eqs. (7)–(8) have to be checked in order to avoid the physically meaningless solutions. The first condition to check is the *indentation condition*. The i th solution $x_{wi}^C, y_{wi}^C, x_{ri}^C, y_{ri}^C$ ($\mathbf{p}_{wi}^{r,C}, \mathbf{p}_{ri}^{r,C}$ in terms of contact points) can be accepted only if the indentation between the wheel surface and the roller surface is negative (with respect to the adopted convection):

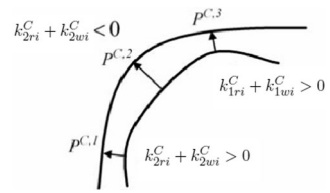
$$p_{ni} = \mathbf{d}_i^{r,C} \cdot \mathbf{n}_r^r(\mathbf{p}_{ri}^{r,C}) \leq 0 \tag{9}$$

where $\mathbf{n}_r^r(\mathbf{p}_{ri}^{r,C})$ is the outgoing normal unitary vector to the roller surface in the candidate solution and $\mathbf{d}_i^{r,C}$ is the distance between $\mathbf{p}_{wi}^{r,C}$ and $\mathbf{p}_{ri}^{r,C}$. Otherwise the solution must be rejected.

The i th solution has to satisfy also the *convexity condition*. This condition constrains the curvature radii of the roller profile to be smaller than the curvature radii of the wheel profile; see Fig. 9. This condition can be expressed by the following relations:

$$k_{1ri}^C + k_{1wi}^C > 0, \quad k_{2ri}^C + k_{2wi}^C > 0 \tag{10}$$

Fig. 9 Curvature condition



where $k_{1ri}^C, k_{1wi}^C, k_{2ri}^C, k_{2wi}^C$ are the normal curvatures of the surfaces in the longitudinal and lateral directions calculated in the candidate solution. The complete expression of surface curvatures is described in [27].

Finally, the solutions with algebraic multiplicity larger than one have to be reduced to a unique solution, rejecting the physically meaningless solutions. As said before, the 4D problem can be reduced to a 1D scalar problem expressing the variables x_w, x_r, y_r as functions of y_w . In order to determine x_w as a function of y_w , the quantity $\frac{x_r}{\sqrt{r(y_r)^2 - x_r^2}}$ can be expressed as a function of x_w, y_w both from the second components of Eq. (7) and from the second components of Eq. (8): $\frac{x_r}{\sqrt{r(y_r)^2 - x_r^2}} = f_1(x_w, y_w), \frac{x_r}{\sqrt{r(y_r)^2 - x_r^2}} = f_2(x_w, y_w)$. Comparing the two expressions ($f_1(x_w, y_w) = f_2(x_w, y_w)$), the following equation can be found:

$$B\sqrt{A^2 - x_w^2} = Cx_w - D, \tag{11}$$

where

$$A = w(y_w), \tag{12}$$

$$B = -G_x r_{33} - y_w r_{12} r_{33} + w(y_w) w'(y_w) r_{13} r_{32} + G_z r_{13} + y_w r_{13} r_{32} - w(y_w) w'(y_w) r_{12} r_{33}, \tag{13}$$

$$C = w(y_w) w'(y_w) r_{11} r_{32} + G_z r_{11} + y_w r_{11} r_{32}, \tag{14}$$

$$D = -G_x w(y_w) w'(y_w) r_{32} + G_z w(y_w) w'(y_w) r_{12}, \tag{15}$$

r_{jk} is the generic element of the rotation matrix $[\mathbf{R}]$, w' is the wheel profile derivative and G_x, G_y, G_z are the components of \mathbf{O}'_w . The solutions of Eq. (11) define x_w as a function of y_w (there are two values of x_w for each value of y_w):

$$x_{w1,2}(y_w) = \frac{CD \pm \sqrt{C^2 D^2 - (C^2 + A^2)(D^2 - A^2 B^2)}}{C^2 + A^2}. \tag{16}$$

At this point, the quantity $\frac{x_r}{\sqrt{r(y_r)^2 - x_r^2}} = f_1(x_{w1,2}(y_w), y_w)$, which is only a function of y_w , can be related to the quantity in $\frac{r(y_r)}{\sqrt{r(y_r)^2 - x_r^2}}$ because:

$$\frac{r(y_r)}{\sqrt{r(y_r)^2 - x_r^2}} = \sqrt{1 + \left(\frac{x_r}{\sqrt{r(y_r)^2 - x_r^2}}\right)^2}; \tag{17}$$

therefore, also $\frac{r(y_r)}{\sqrt{r(y_r)^2 - x_r^2}} = f_3(y_w)$ will be a function of y_w only. Subsequently, to determine y_r as a function of y_w , Eq. (17) can be inserted into the first component of the vectorial

equation (7):

$$r'(y_r)_{1,2} = -f_3(y_w)^{-1} \cdot \frac{x_{w1,2}(y_w)r_{21} - w(y_w)w'(y_w)r_{22} - r_{23}\sqrt{w(y_w)^2 - x_{w1,2}(y_w)^2}}{-w(y_w)w'(y_w)r_{32} - r_{33}\sqrt{w(y_w)^2 - x_{w1,2}(y_w)^2}}. \tag{18}$$

Usually, the function $r'(y_r)$ has a monotonically descending trend; therefore, it can be numerically inverted in order to obtain $y_{r,1,2}(y_w)$; if $r'(y_r)$ is not monotonically descending, the function can still be inverted but a further multiplication of the solution number is needed.

From the second component of Eq. (7) and Eq. (17), $x_{r,1,2}(y_w)$ can be calculated as a function of y_w :

$$x_{r,1,2}(y_w) = \frac{r(y_{r1,2}(y_w))}{f_3(y_w)} \cdot \frac{G_x + x_{w1,2}(y_w)r_{11} + y_w r_{12} - r_{13}\sqrt{w(y_w)^2 - x_{w1,2}(y_w)^2}}{G_z + y_w r_{32} - r_{33}\sqrt{w(y_w)^2 - x_{w1,2}(y_w)^2}}. \tag{19}$$

Finally, replacing the relations $x_{w1,2}(y_w)$, $y_{r,1,2}(y_w)$, $x_{r,1,2}(y_w)$ in the first component of Eq. (8), the following scalar equation can be obtained where the unique unknown is y_w :

$$F_{1,2}(y_w) = -r'(y_{r1,2})r(y_{r1,2})\left(G_z + y_w r_{32} - r_{33}\sqrt{w(y_w)^2 - x_{w1,2}^2} - \sqrt{r(y_r)^2 - x_r^2}\right) - \sqrt{r(y_{r1,2})^2 - x_r^2}\left(G_x + x_{w1,2}r_{11} + y_w r_{12} - r_{13}\sqrt{w(y_w)^2 - x_{w1,2}^2} - y_r\right) = 0. \tag{20}$$

Replacing the solutions y_{wi}^C of the scalar equations $F_1(y_w) = 0$ and $F_2(y_w) = 0$ in Eqs. (16), (18) and (19), the values of the other variables can be obtained:

$$(x_{wi}^C, y_{wi}^C, x_{ri}^C, y_{ri}^C), \quad i = 1, 2, \dots, n, \tag{21}$$

and consequently, the positions of the corresponding contact points on the wheel and on the roller:

$$\mathbf{p}_{wi}^{r,C} = \mathbf{p}_w^r(x_{wi}^C, y_{wi}^C), \mathbf{p}_{ri}^{r,C} = \mathbf{p}_r(x_{ri}^C, y_{ri}^C), \quad i = 1, 2, \dots, n. \tag{22}$$

Since Eq. (11) has irrational terms, the following *analytical conditions* have to be satisfied:

- The solutions $x_{wi}^C, y_{wi}^C, x_{ri}^C, y_{ri}^C$ must be real numbers;
- The solutions must not generate complex terms by means of the radicals;
- The solutions of Eq. (20) have to be effective solutions of Eqs. (7) and (8) (they might not be valid due to removal of the radicals by squaring).

The second part of the contact model is the adhesion model. For each contact point calculated by the previous method, it is necessary to compute the forces and the torque applied on the wheelset. The procedure used in this work consists of two different steps: the normal problem and the tangential problem. The normal contact problem has been solved according to the Hertz theory while the tangential contact forces and the spin moment have been calculated by means of the Kalker linear theory [32, 33].

In particular, the Hertz theory allows evaluating the normal contact force in the contact point as follows:

$$N = k_h |p_n|^\gamma - k_v V_n, \tag{23}$$

where

- $V_{sl,n}$ is the normal component of the penetration velocity $V_n = \mathbf{V}_w^r \cdot \mathbf{n}_r^r(\mathbf{P}_r^r, C)$ and \mathbf{V}_w^r is the velocity of the contact point rigidly connected to the wheel (referred to the roller system);
- p_n is the penetration between roller and wheel (see Eq. (9));
- k_h is the Hertz constant (depending on the materials, the contact area dimensions and the surface curvatures);
- k_v is the damping contact constant.

Hertz theory allows also evaluating the ellipse semi-axes a and b that are functions of the curvatures and of the material properties. According to the linear Kalker theory, the longitudinal component of the tangential force T_x^* , the lateral component of the tangential force T_y^* and the spin moment M_{sp} can be evaluated as follows:

$$T_x^* = -f_{11}\varepsilon_x, \quad T_y^* = -f_{22}\varepsilon_y - f_{23}\varepsilon_{sp}, \quad M_{sp} = f_{23} - f_{33}\varepsilon_{sp}, \quad (24)$$

with

$$f_{11} = abGC_{11}, \quad f_{22} = abGC_{22}, \quad f_{23} = ab^{3/2}GC_{23}, \quad f_{33} = ab^2GC_{33}, \quad (25)$$

where

- G is the shear modulus;
- C_{ij} are the Kalker coefficient tabulated with respect to the Poisson’s coefficient and to the ratio a/b ;
- a, b are the ellipse semi-axes;
- $\varepsilon_x, \varepsilon_y, \varepsilon_{sp}$ represent the virtual creepages $\varepsilon_x = (\mathbf{V}_w^r \cdot \mathbf{i}_r)/v_{ow}$, $\varepsilon_y = (\mathbf{V}_w^r \cdot \mathbf{t}_r)/v_{ow}$ and $\varepsilon_{sp} = (\omega_w^r \cdot \mathbf{n}_r)/v_{ow}$ where v_{ow} is the magnitude of the wheelset centre of mass velocity, and ω_{sl} is the wheelset angular velocity;
- $\mathbf{i}_r, \mathbf{t}_r$ and \mathbf{n}_r are the three fundamental unitary vectors (longitudinal, transversal and normal) of the wheel surface.

The above description is referred to as the linear theory of Kalker that is applicable only in case of limited sliding; therefore, the total creep force $T^* = \sqrt{(T_x^*)^2 + (T_y^*)^2}$ has to be saturated so that the resultant force does not exceed the pure slip value depending on the adhesion coefficient, $T_S = \mu N$. If the creep force saturation coefficient ξ is defined as follows:

$$\xi = \frac{T_S}{T^*} \left[\left(\frac{T^*}{T_S} \right) - \frac{1}{3} \left(\frac{T^*}{T_S} \right)^2 + \frac{1}{27} \left(\frac{T^*}{T_S} \right)^3 \right] \quad \text{if } T^* \leq 3T_S, \quad (26a)$$

$$\xi = \frac{T_S}{T^*} \quad \text{if } T^* > 3T_S, \quad (26b)$$

the saturated creep forces in longitudinal and lateral directions are given by:

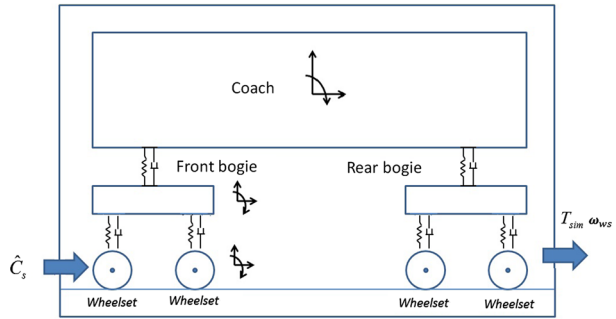
$$T_x = \xi T_x^*, \quad (27a)$$

$$T_y = \xi T_y^*. \quad (27b)$$

3.2 The virtual railway vehicle model

The virtual railway vehicle model simulates the dynamical behaviour of the railway vehicle during a braking phase under degraded adhesion conditions. The model, designed for a real-time implementation, is composed of two parts: the 2D vehicle model and the 2D adhesion

Fig. 10 The virtual railway vehicle model



model. The inputs are the 4 estimated torques \hat{C}_s to be applied to the wheelsets while the outputs are the 4 simulated tangential contact forces T_{sim} and the 4 simulated wheel angular velocities ω_{ws} .

3.2.1 The virtual vehicle model

The 2D vehicle model of the considered railway vehicle (UIC-Z1 coach) is a simplified 2D multibody model of the longitudinal train dynamics (only 3 DOFs for each body are taken into account) [14]. The model (see Fig. 10) consists of a carbody, two bogies and four wheelsets, held by the primary and secondary suspensions. Starting from the estimated torques \hat{C}_s , the model evaluates the kinematic variables of the 4 wheelsets v_{ws} , ω_{ws} and the 4 normal contact forces N_{cs} to be passed to the adhesion model and receives the 4 tangential contact forces T_{sim} .

3.2.2 The adhesion model

The adhesion model has been especially developed to describe degraded adhesion conditions [19, 34–37] and calculates, for all the 4 wheelset–rail pairs, the tangential contact forces T_{sim} starting from the wheelset kinematic variables v_{ws} , ω_{ws} and the normal contact forces N_{cs} (see Fig. 11).

The main phenomena characterising the degraded adhesion are the large sliding occurring at the contact interface and, consequently, the high energy dissipation. Such a dissipation causes a cleaning effect on the contact surfaces, and finally an adhesion recovery due to the removal of the external contaminants. When the specific dissipated energy W_{sp} is low, the cleaning effect is almost absent, the contaminant level h does not change, and the adhesion coefficient f is equal to its original value f_d in degraded adhesion conditions f_d . As the energy W_{sp} increases, the cleaning effect increases too, the contaminant level h becomes thinner, and the adhesion coefficient f rises. In the end, for large values of W_{sp} , all the contaminant is removed (h is null) and the adhesion coefficient f reaches its maximum value f_r ; the adhesion recovery due to the removal of external contaminants is now completed. At the same time, if the energy dissipation begins to decrease, due to a, for example, lower sliding, the reverse process occurs (see Fig. 11).

Since the contaminant level h and its characteristics are usually totally unknown, it is useful to try to experimentally correlate the adhesion coefficient f directly with the specific dissipated energy W_{sp} :

$$W_{sp} = T_{sim}e = f N_{cs}e f = \frac{T_{sim}}{N_{cs}} \quad (28)$$

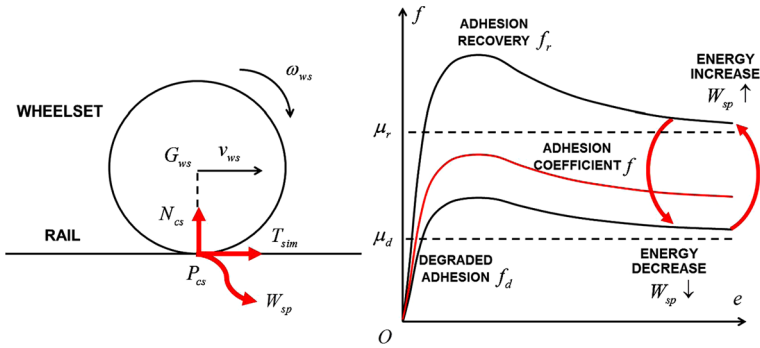


Fig. 11 The adhesion model

where the creepage e is defined as

$$e = \frac{s}{v_{ws}} = \frac{v_{ws} - r_w \omega_{ws}}{v_{ws}}, \tag{29}$$

s is the sliding and r_w is the wheel radius. This way the specific dissipated energy W_{sp} can also be interpreted as the energy dissipated at the contact for unit of distance travelled by the railway vehicle.

To reproduce the qualitative trend previously described and to allow the adhesion coefficient to vary between the extreme values f_d and f_r , the following expression for f is proposed:

$$f = [1 - \lambda(W_{sp})]f_d + \lambda(W_{sp})f_r \tag{30}$$

where $\lambda(W_{sp})$ is an unknown transition function between degraded adhesion and adhesion recovery while the adhesion levels f_d, f_r can be evaluated according to [31–33, 38–40] as functions of e, N_{cs} and the track friction coefficients μ_d, μ_r (corresponding to degraded adhesion and full adhesion recovery, respectively). The function $\lambda(W_{sp})$ has to be positive and monotonously increasing; moreover, the following boundary conditions are supposed to be verified: $\lambda(0) = 0$ and $\lambda(+\infty) = 1$.

This way, the authors suppose that the transition between degraded adhesion and adhesion recovery only depends on W_{sp} . This hypothesis is obviously only an approximation but, as it will be clearer in the next sections, it describes the adhesion behaviour well. Initially, to catch the physical essence of the problem without introducing a large number of unmanageable and unmeasurable parameters, the authors have chosen the following simple expression for $\lambda(W_{sp})$:

$$\lambda(W_{sp}) = 1 - e^{-\tau W_{sp}} \tag{31}$$

where τ is now the only unknown parameter to be tuned on the basis of the experimental data (in this case $\tau = 1.9 \cdot 10^{-4}$ m/J) [16, 19, 41, 42].

In this research activity, the two main adhesion coefficients f_d and f_r (degraded adhesion and adhesion recovery) have been calculated according to Polach [30–33, 38–40]:

$$\begin{aligned}
 f_d &= \frac{2\mu_d}{\pi} \left[\frac{k_{ad}\varepsilon_d}{1 + (k_{ad}\varepsilon_d)^2} + \arctan(k_{sd}\varepsilon_d) \right], \\
 f_r &= \frac{2\mu_r}{\pi} \left[\frac{k_{ar}\varepsilon_r}{1 + (k_{ar}\varepsilon_r)^2} + \arctan(k_{sr}\varepsilon_r) \right]
 \end{aligned}
 \tag{32}$$

where

$$\varepsilon_d = \frac{2}{3} \frac{C\pi a^2 b}{\mu_d N_c} e, \quad \varepsilon_r = \frac{2}{3} \frac{C\pi a^2 b}{\mu_r N_c} e.
 \tag{33}$$

The quantities k_{ad} , k_{sd} and k_{ar} , k_{sr} are the Polach reduction factors (for degraded adhesion and adhesion recovery, respectively) and μ_d , μ_r are the friction coefficients defined as follows:

$$\mu_d = \left(\frac{\mu_{cd}}{A_d} - \mu_{cd} \right) e^{-\gamma_d s} + \mu_{cd}, \quad \mu_r = \left(\frac{\mu_{cr}}{A_r} - \mu_{cr} \right) e^{-\gamma_r s} + \mu_{cr}
 \tag{34}$$

in which μ_{cd} , μ_{cr} are the kinetic friction coefficients, A_d , A_r are the ratios between the kinetic friction coefficients and the static ones, and γ_d , γ_r are the friction decrease rates. The Polach approach (see Eq. (32)) has been followed since it permits describing the decrease of the adhesion coefficient with increasing creepage and better fitting the experimental data (see Fig. 11).

Finally, it has to be noticed that the semi-axes a and b of the contact patch (see Eq. (33)) depend only on the material properties, the contact point position P_c on wheel and rail (through the curvatures of the contact surfaces in the contact point) and the normal force N_c , while the contact shear stiffness C (N/m³) is a function only of material properties, the contact patch semi-axes a and b and the creepages. More particularly, the following relation holds [30]:

$$C = \frac{3G}{8a} \sqrt{\left(c_{11} \frac{e_x}{e} \right)^2 + \left(c_{22} \frac{e_y}{e} \right)^2}
 \tag{35}$$

where $c_{11} = c_{11}(\sigma, a/b)$ and $c_{22} = c_{22}(\sigma, a/b)$ are the Kalker coefficients.

In the end, the desired values of the adhesion coefficient f and of the tangential contact force $T_{sim} = f N_{cs}$ can be evaluated by solving the nonlinear algebraic Eq. (30) in which the explicit expression of W_{sp} has been inserted (see Eq. (28)):

$$f = \mathfrak{S}(f, t)
 \tag{36}$$

where \mathfrak{S} indicates the generic functional dependence. Due to the simplicity of the transition function $\lambda(W_{sp})$, the solution can be easily obtained through standard nonlinear solvers [43].

3.3 The controllers

The controllers have to reproduce on the roller-rig the dynamical behaviour of the virtual railway vehicle under degraded adhesion conditions in terms of angular velocities ω_w , applied torques C_s and, consequently, tangential contact forces $T_c^{l/r}$. The inputs of the controller are the simulated tangential forces T_{sim} , the simulated wheelset angular velocities

ω_{ws} , the estimated wheel angular velocities $\widehat{\omega}_w$, the estimated motor torques \widehat{C}_s and the roller angular velocities $\omega_r^{l/r}$. The outputs are the 8 roller control torques $u^{l/r}$.

The controller layout consists of 8 independent controllers (one for each roller) and makes use of a sliding mode strategy based on the dynamical equations of the roller rig; this way, it is possible to reduce the disturbance effects due to the system nonlinearities and the parameter uncertainties [20, 21]. The total control torques $u^{l/r}$ are defined as

$$u^{l/r} = u_{\text{cont}}^{l/r} + u_{\text{disc}}^{l/r} + u_{\text{diff}}^{l/r} \tag{37}$$

where the continuous control part $u_{\text{cont}}^{l/r}$ is built starting from the approximated 1D models of wheelset and rollers and by supposing the slidings between the contact surfaces negligible (on the roller-rig the adhesion conditions are good, with a friction coefficient μ_{roll} equal to 0.3):

$$\begin{aligned} C_s &= J_w \dot{\omega}_w - T_c^l r_w - T_c^r r_w, \\ u^l &= J_r \dot{\omega}_r^l - T_c^l r_w, & u^r &= J_r \dot{\omega}_r^r - T_c^r r_w, \\ \omega_r^l &= -\frac{r_w}{r_r} \omega_w, & \dot{\omega}_r^l &= -\frac{r_w}{r_r} \dot{\omega}_w, \\ \omega_r^r &= -\frac{r_w}{r_r} \omega_w, & \dot{\omega}_r^r &= -\frac{r_w}{r_r} \dot{\omega}_w \end{aligned} \tag{38}$$

in which r_r, r_w are the roller and wheelset radii and J_r, J_w are their inertias. By removing T_c^l and T_c^r in Eq. (38), the following relation is obtained:

$$C_s - \frac{r_w}{r_r} (u^l + u^r) = J_{\text{tot}} \dot{\omega}_w J_{\text{tot}} = J_w + 2 \left(\frac{r_w}{r_r} \right)^2 J_r \tag{39}$$

where J_{tot} is the total inertia of the rollers and the wheelset reduced to the wheelset rotation axis. Subsequently, the desired wheelset dynamics is considered as

$$\widehat{C}_s = J_w \dot{\omega}_{ws} + T_{\text{sim}} r_w, \tag{40}$$

together with the sliding surface $S = \omega_{ws} - \omega_w = 0$ and its time derivative $\dot{S} = \dot{\omega}_{ws} - \dot{\omega}_w$. If the torque estimation $\widehat{C}_s \simeq C_s$ is accurate enough, the sliding condition $\dot{S} = 0$ can be obtained, starting from Eqs. (39) and (40), by taking

$$\begin{aligned} u &= \frac{r_r}{r_w} \left[\left(1 - \frac{J_{\text{tot}}}{J_s} \right) \widehat{C}_s + \frac{J_{\text{tot}}}{J_s} T_{\text{sim}} r_w \right], \\ u^l &= \frac{u}{2}, & u^r &= \frac{u}{2}. \end{aligned} \tag{41}$$

On the other hand, $u_{\text{disc}}^{l/r}$ is the discontinuous control part related to the rejection of the disturbances:

$$u_{\text{disc}}^l = u_{\text{disc}}^r = k \Re(\omega_{ws} - \widehat{\omega}_w). \tag{42}$$

The discontinuous controls $u_{\text{disc}}^{l/r}$ are characterised by the gain k and the function \Re shown in Fig. 12 (the dead zone amplitude δ and the slope σ are control parameters to be tuned).

Finally, $u_{\text{diff}}^{l/r}$ is an auxiliary control part aimed at synchronising the roller angular velocities ω_r^l, ω_r^r :

$$u_{\text{diff}}^l = -k_d \Re(\omega_r^l - \omega_r^r), \quad u_{\text{diff}}^r = k_d \Re(\omega_r^l - \omega_r^r). \tag{43}$$

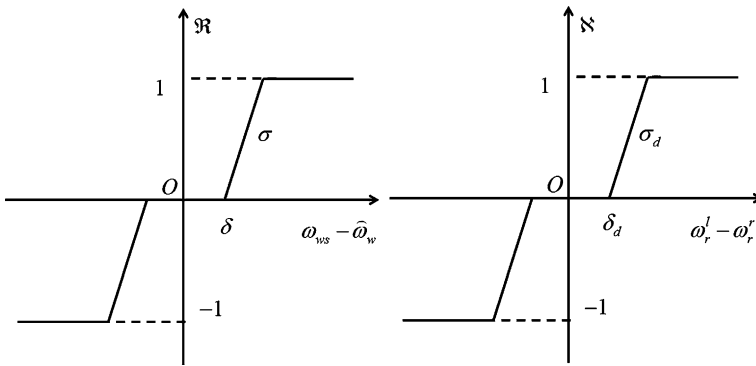


Fig. 12 Discontinuous and auxiliary control characteristics

The function \mathfrak{K} is reported in Fig. 12, while the parameters k_d , δ_d and σ_d have to be tuned. The controller performances will be evaluated by means of the angular velocity error $e_\omega = \omega_{ws} - \omega_w$ and the torque estimation error $e_c = \hat{C}_s - C_s$. Limited values of the previous errors e_ω , e_c assure a good estimation of the tangential contact forces $T_c^{l/r}$.

3.4 The torque estimators

The estimators aim at evaluating the wheelset angular velocities $\hat{\omega}_w$ and the torques applied to the wheelset \hat{C}_s starting from the roller angular velocities $\omega_r^{l/r}$ and the longitudinal reaction forces $T_{mis}^{l/r}$ on the roller supports. Since the slidings between wheelset and rollers can be neglected, the following estimations approximately hold:

$$\hat{\omega}_w = -\frac{r_r}{r_w} \frac{\omega_r^l + \omega_r^r}{2}, \quad \hat{\dot{\omega}}_w = -\frac{r_r}{r_w} \frac{\dot{\omega}_r^l + \dot{\omega}_r^r}{2}, \quad \hat{T}_c^{l/r} = T_{mis}^{l/r}. \tag{44}$$

Of course, the derivative operation $\frac{d}{dt}$ has to be robust, taking into account the numerical noise affecting $\omega_r^{l/r}$. At this point, to estimate the motor torque applied to the wheelset, the estimator employs the simplified dynamical model of the wheelset:

$$\hat{C}_s = J_w \hat{\dot{\omega}}_w - \hat{T}_c^l r_w - \hat{T}_c^r r_w. \tag{45}$$

It is worth noting that, in this kind of applications, the estimators have to be necessarily simple because they are thought for a real-time implementation and, at the same time, the physical characteristics of the railway vehicle on the roller-rig are generally unknown.

3.5 The numerical implementation of the model

Concerning computational load and memory consumption, the only parts of the HIL architecture (see Fig. 1) that have to run in real-time are the virtual railway vehicle model, the controllers and the torque estimators. The numerical models related to these parts are quite simple and fast, and allow a good compromise between accuracy and efficiency. During the preliminary tests of the proposed HIL system, the efficiency of the previous models enabled the use of fixed step numerical integrators (in particular, the Dormand–Prince ODE5 integrator [44]). The main features of the chosen integrator are summarised in Table 5.

Table 5 Characteristics of the numerical integrator

Integrator	Implemented algorithm	Order	Step [s]
ODE5	Dormand–Prince	fixed, 5th order	fixed, 10^{-4}

The choice of the integration step is mainly due to the stiffness of the contact and adhesion models inside the virtual railway vehicle model and to the delays characterising controllers and actuators. Such an integrator, up to now, turned out to be quite effective and robust in facing the problems caused by the stiffness, delays and the noise typical of these systems.

4 Experimental data

The HIL model performance have been validated by means of the comparison with the experimental data, provided by Trenitalia S.p.A. [16] and coming from on-track braking tests carried out in Velim (Czech Republic) with the coach UIC-Z1 [14]. The considered vehicle is equipped with a fully-working WSP system [15]. These experimental tests have been carried out on a straight railway track. The wheel profile is the ORE S1002 (with a wheelset width d_w equal to 1.5 m) while the rail profile is the UIC60 (with a gauge d_r equal to 1.435 m and a laying angle α_p equal to $1/20$ rad).

The main characteristics of the braking test, considered as benchmark in this paper, are summarised in Table 6 (comprising the main wheel, rail and contact parameters; see Sect. 3.2.2) [31–33, 38–40, 45]. The value of the kinetic friction coefficient under degraded adhesion conditions μ_{cd} depends on the test performed on the track; the degraded adhesion conditions are usually reproduced using a watery solution containing surface-active agents, e.g. a solution sprinkled by a specially provided nozzle directly on the wheel–rail interface on the first wheelset in the running direction. The surface-active agent concentration in the solution varies according to the type of test and the desired friction level. The value of the kinetic friction coefficient under full adhesion recovery μ_{cr} corresponds to the classical kinetic friction coefficient under dry conditions.

During the preliminary tests of the proposed HIL system, the physical parameters of the adhesion model were identified through suitable tests performed on railway lines (see [14–16, 41]) and on test-rigs (see [17]). In some cases, the first attempt values of the physical parameters were initially taken from the literature (see [31, 38]).

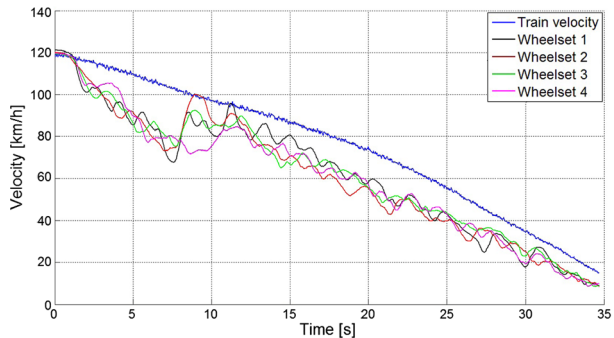
First, the vehicle and wheelset velocities v^{sp} , $v_{wi}^{sp} = r_w \omega_{wi}^{sp}$ ($i = 1, \dots, 4$) are taken into account (see Fig. 13). Both the WSP intervention and the adhesion recovery in the second part of the braking maneuver are clearly visible. Second, the slidings among the wheelsets and the rails have been considered: $s_i^{sp} = v^{sp} - r_w \omega_{wi}^{sp} = v^{sp} - v_{wi}^{sp}$ (see Figs. 16, 17, 18, and 19). However, these physical quantities cannot be locally compared to each other because of the complexity and the chaoticity of the system due to, for instance, the presence of discontinuous and threshold elements like the WSP. To better evaluate the behaviour of s_i^{sp} from a global point of view, it is useful to introduce the statistical means \bar{s}_i^{sp} and the standard deviations Δ_i^{sp} of the considered variables:

$$\begin{aligned} \bar{s}_i^{sp} &= \frac{1}{T_F - T_I} \int_{T_I}^{T_F} s_i^{sp} dt, \\ \Delta_i^{sp} &= \sqrt{\frac{1}{T_F - T_I} \int_{T_I}^{T_F} (s_i^{sp} - \bar{s}_i^{sp})^2 dt} \end{aligned} \tag{46}$$

Table 6 Main wheel, rail and contact parameters

Parameter	Units	Value
Initial train velocity V	km/h	120
Nominal braking torque C	N m	9500
Measurement sample time Δt_s	s	0.01
Young modulus	[Pa]	$2.1 \cdot 10^{11}$
Shear modulus	[Pa]	$8.0 \cdot 10^{10}$
Poisson coefficient	[N s/m]	0.3
Contact damping constant	–	$1.0 \cdot 10^5$
Polach reduction factor k_{ad}	–	0.3
Polach reduction factor k_{sd}	–	0.1
Polach reduction factor k_{ar}	–	1.0
Polach reduction factor k_{sr}	–	0.4
Kinetic friction coefficient (degraded adhesion) μ_{cd}	–	0.06
Kinetic friction coefficient (adhesion recovery) μ_{cr}	–	0.28
Friction ratio A_d	–	0.40
Friction ratio A_r	–	0.40
Friction decrease rate γ_d	[s/m]	0.20
Friction decrease rate γ_r	[s/m]	0.60

Fig. 13 Experimental vehicle and wheelset velocities v^{SP} , $v_{wi}^{SP} = r_w \omega_{wi}^{SP}$



where T_I and T_F are respectively the initial and final times of the simulation (see Table 8).

5 The model validation

In this section, the whole HIL architecture model is simulated and validated. More precisely, both the dynamical and the control performances of the system will be analysed. The main control parameters are summarised in Table 7 (see Sect. 3.3) [44]. The simulated vehicle and wheelset velocities $v_s, v_{wsi} = r_w \omega_{wsi}$ are reported in Fig. 14. Figures 13 and 14 highlight a good qualitative match between experimental and simulated data, both concerning the WSP intervention and the adhesion recovery in the second part of the braking maneuver. The direct comparison between the experimental and simulated train velocities v^{SP}, v_s is illustrated in Fig. 15 and shows also a good quantitative agreement between the considered

Table 7 Main control parameters

Parameter	Units	Value
Control gain k	N m	$2 \cdot 10^4$
Dead zone amplitude δ	rad/s	0.05
Control slope σ	N m s/rad	10
Control gain k_d	N m	$2 \cdot 10^4$
Dead zone amplitude δ_d	rad/s	0.05
Control slope σ_d	N m s/rad	10

Fig. 14 Simulated vehicle and wheelset velocities v_s , $v_{wsi} = r_w \omega_{wsi}$

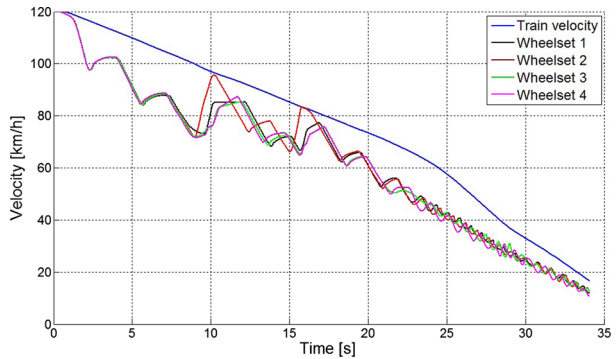
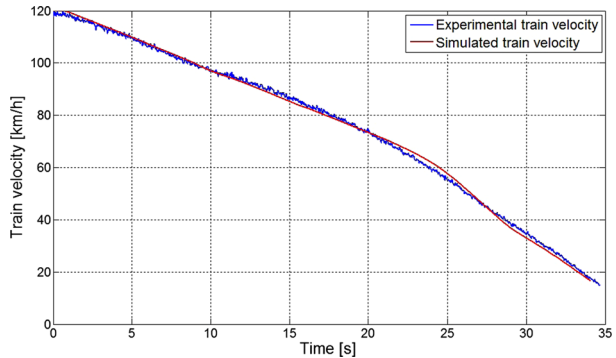


Fig. 15 Experimental and simulated train velocities v^{SP} , v_s



quantities. Subsequently, according to Sect. 4, the simulated slidings among wheelsets and rails $s_{si} = v_s - r_w \omega_{wsi} = v_s - v_{wsi}$ are taken into account and compared to the experimental ones s_i^{SP} (see Figs. 16, 17, 18, and 19).

The match between experimental and simulated slidings is qualitatively good. However, since these physical quantities cannot be locally compared to each other because of the complexity and the chaoticity of the system, the statistical means \bar{s}_{si} and the standard deviations Δ_{si} of the simulated slidings s_{si} are introduced (according to Eq. (46)) to better evaluate the global behaviour of analysed variables. The comparison between experimental \bar{s}_i^{SP} , Δ_i^{SP} and simulated \bar{s}_{si} , Δ_{si} statistical indices is reported in Table 8 and highlights also a good quantitative match between the studied quantities. The controller performances are evaluated in terms of angular velocity error $e_\omega = \omega_{ws} - \omega_w$ and the torque estimation error $e_c = \hat{C}_s - C_s$. Small values of the errors e_ω , e_c assure a good estimation of the tangential contact forces $T_c^{l/r}$. The time history of the angular velocity error e_ω is plotted in Fig. 20 and shows the

Fig. 16 Experimental and simulated train slidings s_1^{SP} , $s_{s,1}$ for the first wheelset

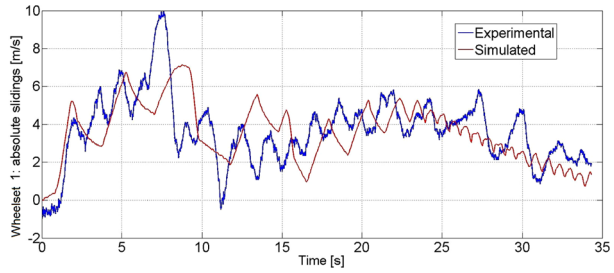


Fig. 17 Experimental and simulated train slidings s_2^{SP} , $s_{s,2}$ for the second wheelset

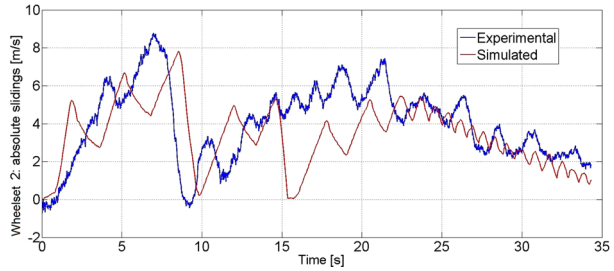


Fig. 18 Experimental and simulated train slidings s_3^{SP} , $s_{s,3}$ for the third wheelset

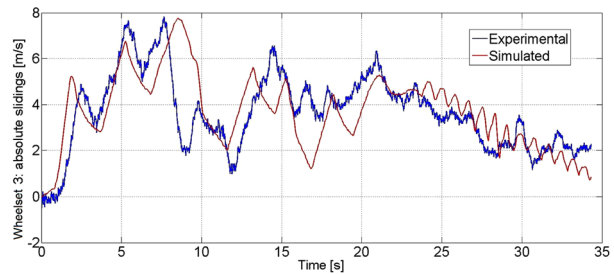
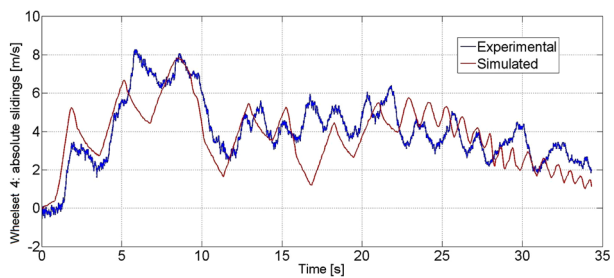


Fig. 19 Experimental and simulated train slidings s_4^{SP} , $s_{s,4}$ for the fourth wheelset



control capability of stabilising the system and rejecting the disturbances produced by the initial transient and the adhesion recovery in the second phase of the braking manoeuvre. The torque estimation error $e_c = \hat{C}_s - C_s$ and the real torques applied to the wheelset C_s are respectively reported in Figs. 21 and 22. Also in this case, the controllers turn out to be effective in reproducing the real torques applied to the wheelsets of the vehicle. Finally, the result analysis highlights the control capability of reproducing on the roller-rig a generic wheel-rail degraded adhesion pattern calculated by the reference virtual railway vehicle model (in

Table 8 Experimental \bar{s}_i^{SP} , Δ_i^{SP} and simulated \bar{s}_{si} , Δ_{si} statistical indices

Wheelset	\bar{s}_i^{SP} [km/h]	\bar{s}_{si} [km/h]	Δ_i^{SP} [km/h]	Δ_{si} [km/h]
Wheelset 1	13.08	12.82	6.45	6.56
Wheelset 2	13.36	12.88	7.25	6.95
Wheelset 3	13.09	13.32	5.92	5.70
Wheelset 4	13.52	13.59	6.22	5.82

Fig. 20 Angular velocity error

$$e_\omega = \omega_{ws} - \omega_w$$

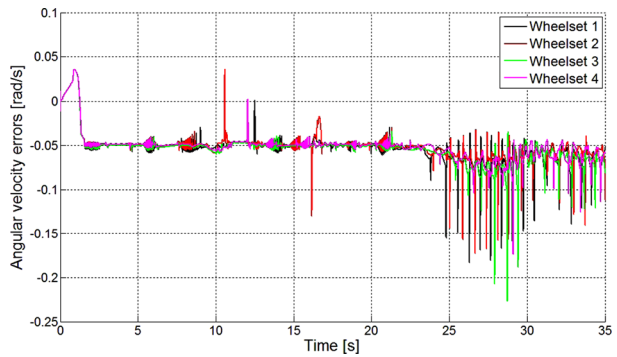
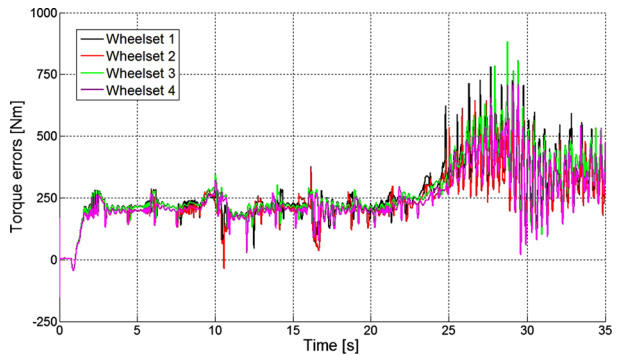


Fig. 21 Torque estimation error

$$e_c = \hat{C}_s - C_s$$

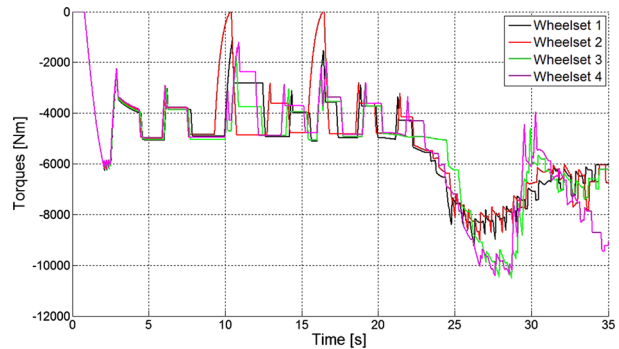


terms of angular velocities ω_w , applied torques on the wheelsets C_s and, consequently, in terms of tangential efforts $T_c^{l/r}$ exchanged between the wheelsets and the rails).

6 Conclusions and further developments

In this work, the authors described an innovative Hardware In the Loop (HIL) architecture to test braking onboard subsystems on full-scale roller-rigs under good and degraded adhesion conditions. The new strategy allows reproducing on the roller-rig a generic wheel–rail adhesion pattern and, in particular, degraded adhesion conditions. An accurate multibody model of the whole system has been developed, including an innovative contact model to describe the wheel–roller interaction. The proposed approach has been preliminarily validated through the experimental data provided by Trenitalia and highlighted good performance in reproducing on the roller-rig the complex interaction between degraded adhesion conditions and railway vehicle dynamics during the braking manoeuvre.

Fig. 22 Torque applied to the wheelset C_s



Many further developments of this research activity are scheduled for the future and will regard the implementation of the control strategy and the virtual vehicle model on the Firenze-Osmannoro roller-rig. This way, firstly a further validation of the proposed HIL approach will be possible through experimental tests performed directly on the roller-rig. The new tests, currently on-going, will allow a deeper investigation of the degraded adhesion model and an improvement of the model parameters identification. Subsequently, the whole HIL system will be employed to design and test new on board subsystems such as WSP, antiskid, etc.

7 Disclosure of potential conflicts of interest

The authors declare that they have no conflict of interest. Furthermore, the authors did not receive funding from any agencies.

References

1. Jaschinski, A., Chollet, H., Iwnicki, S.: The application of the roller rigs to railway vehicle dynamics. *Veh. Syst. Dyn.* **31**, 325–344 (1999)
2. Dukkipati, R.: A parametric study of the lateral stability of a railway bogie on a roller rig. In: *Proceedings of the Institution of Mechanical Engineering Part F*, vol. 213, pp. 39–47 (1999)
3. Ahn, K., Park, J., Ryew, S.: The construction of a full-scale wheel/rail roller rig in Korea. In: *Proceedings of the IEEE International Conference on Automation Science and Engineering (CASE)*, pp. 802–803 (2012)
4. Lee, N., Kang, C., Lee, W., Dongen, T.: Roller rig tests of a semi-active suspension system for a railway vehicle. In: *Proceedings of the IEEE International Conference on Control, Automation and Systems (ICCAS)*, pp. 117–122 (2012)
5. Dukkipati, R.V.: Lateral stability analysis of a railway truck on roller rig. *Mech. Mach. Theory* **36**, 189–204 (2001)
6. Zhang, W., Chen, J., Wu, X., Jin, X.: Wheel/rail adhesion and analysis by using full scale roller rig. *Wear* **253**, 82–88 (2002)
7. Allotta, B., Conti, R., Meli, E., Pugi, L., Ridolfi, A.: Development of an HIL railway roller rig model for the traction and braking testing activities under degraded adhesion conditions. *Int. J. Non-Linear Mech.* **57**, 50–64 (2013)
8. Malvezzi, M., Allotta, B., Pugi, L.: Feasibility of degraded adhesion tests in a locomotive roller rig. In: *Proceedings of the Institution of Mechanical Engineering Part F*, vol. 222, pp. 27–43 (2008)
9. Bosso, N., Zampieri, N.: Real-time implementation of a traction control algorithm on a scaled roller-rig. *Veh. Syst. Dyn.* **51**(4), 517–541 (2013)

10. Spiryagin, M., Sun, Y.Q., Cole, C., Mc Sweeney, T., Simson, S., Persson, I.: Development of a real-time bogie test-rig model based on railway specialised multibody software. *Veh. Syst. Dyn.* **51**(2), 236–250 (2013)
11. Bosso, N., Gugliotta, A., Soma, A., Spiryagin, M.: Adhesion force estimation on 1/5 scaled test rig. In: Proceedings of the ECCOMAS Multibody Dynamics Conference, Warsaw, Poland (2009)
12. Bosso, N., Gugliotta, A., Soma, A., Spiryagin, M.: Methodology for the determination of wheel–roller friction coefficient on 1/5 scaled test rig. In: Proceedings of the 8th International Conference on Contact Mechanics and Wear of Roller/Wheel Systems (CM2009), Florence, Italy (2009)
13. www.mathworks.com. Official Site of Mathworks. Natick (2013)
14. Trenitalia SpA: UIC-Z1 coach. Internal Report of Trenitalia (2000)
15. Trenitalia SpA: WSP system. Internal Report of Trenitalia (2005)
16. Trenitalia SpA: On-track braking tests. Internal Report of Trenitalia (2006)
17. Trenitalia SpA: Full-scale roller-rig: technical documentation. Internal Report of Trenitalia (2011)
18. SICME Motori: IPM synchronous motor datasheet. Internal Report of SICME Motori (2010)
19. Meli, E., Ridolfi, A.: An innovative wheel–rail contact model for railway vehicles under degraded adhesion conditions. *Multibody Syst. Dyn.* **33**, 285–313 (2014)
20. Sontag, E.D.: *Mathematical Control Theory*. Springer, New York (1998)
21. Khalil, H.K.: *Nonlinear Systems*. Prentice Hall, New York (2002)
22. Allotta, B., Pugi, L., Ridolfi, A., Malvezzi, M., Vettori, G., Rindi, A.: Evaluation of odometry algorithm performance using railway vehicle dynamic model. *Veh. Syst. Dyn.* **50**, 699–724 (2012)
23. Krishnan, R.: *Permanent Magnet Synchronous and Brushless DC Motor Drives*. CRC Press, Taylor & Francis (2010)
24. Vagati, A., Pellegrino, G., Guglielmi, P.: Design tradeoff between constant power speed range, uncontrolled generator operation and rated current of IPM motor drives. *IEEE Trans. Ind. Appl.* **47**, 1995–2003 (2011)
25. Li, S., Xia, C., Zhou, X.: Disturbance rejection control method for permanent magnet synchronous motor speed-regulation system. *Mechatronics* **22**, 706–714 (2012)
26. Vu, N.T., Choi, H.H., Jung, J.: Certainty equivalence adaptive speed controller for permanent magnet synchronous motor. *Mechatronics* **22**, 811–818 (2012)
27. Malvezzi, M., Meli, E., Rindi, A., Falomi, S.: Determination of wheel–rail contact points with semianalytic method. *Multibody Syst. Dyn.* **20**, 327–358 (2008)
28. Malvezzi, M., Meli, E., Falomi, S.: Multibody modeling of railway vehicles: innovative algorithms for the detection of wheel–rail contact points. *Wear* **271**, 453–461 (2011)
29. Magheri, S., Malvezzi, M., Meli, E., Falomi, S., Rindi, A.: An innovative wheel–rail contact model for multibody applications. *Wear* **271**, 462–471 (2011)
30. Kalker, J.J.: *Three-Dimensional Elastic Bodies in Rolling Contact*. Kluwer Academic, Norwell (1990)
31. Polach, O.: Creep forces in simulations of traction vehicles running on adhesion limit. *Wear* **258**, 992–1000 (2005)
32. Pombo, J., Ambrosio, J.: Application of a wheel–rail contact model to railway dynamics in small radius curved tracks. *Multibody Syst. Dyn.* **19**, 91–114 (2008)
33. Pombo, J., Silva, A.J.: A new wheel–rail contact model for railway dynamics. *Veh. Syst. Dyn.* **45**, 165–189 (2007)
34. Blau, P.J.: Embedding wear models into friction models. *Tribol. Lett.* **34**, 75–79 (2009)
35. Boiteux, M.: Le probleme de l’adherence en freinage. In: *Revue generale des chemins de fer*, pp. 59–72 (1986)
36. Voltr, P., Lata, M., Cerny, O.: Measuring of wheel–rail adhesion characteristics at a test stand. In: Proceedings of XVIII Conference on Engineering Mechanics (2012)
37. Pérez, A.T., Fatjó, G.G., Hadfield, M., Austen, S.: A model of friction for a pin-on-disc configuration with imposed pin rotation. *Mech. Mach. Theory* **46**, 1755–1772 (2011)
38. Polach, O.: A fast wheel–rail forces calculation computer code. *Veh. Syst. Dyn.* **33**, 728–739 (1999)
39. Shabana, A.A., Zaza, K.E., Escalona, J.E., Sany, J.R.: Development of elastic force model for wheel/rail contact problems. *J. Sound Vib.* **269**, 295–325 (2004)
40. Shabana, A.A., Tobaa, M., Sugiyama, H., Zaazaa, K.E.: On the computer formulations of the wheel/rail contact problem. *Nonlinear Dyn.* **40**, 169–193 (2005)
41. Allotta, B., Meli, E., Ridolfi, A., Rindi, A.: Development of an innovative wheel–rail contact model for the analysis of degraded adhesion in railway systems. *Tribol. Int.* **69**, 128–140 (2013)
42. Nocedal, J., Wright, S.: *Numerical Optimization*. Springer Series in Operation Research. Berlin (1999)
43. Kelley, C.: *Iterative Methods for Linear and Nonlinear Equations*. SIAM, Philadelphia (1995)
44. Shampine, L., Reichelt, M.: The Matlab ODE suite. *SIAM J. Sci. Comput.* **18**, 1–22 (1997)
45. UNI-EN: *Railway applications, Braking-Wheel Sliding Protection*. UNI-EN 15595 (2009)